PHYSICAL REVIEW E **106**, 045308 (2022)

Color-gradient lattice Boltzmann model for immiscible fluids with density contrast

A. Subhedar[*]
Department of Chemical Engineering, Indian Institute of Technology Bombay, Powai,
Mumbai 400076, India

(Received 7 June 2021; revised 21 June 2022; accepted 30 August 2022; published 21 October 2022)

We present a color-gradient-based lattice Boltzmann model for immiscible fluids with a large density contrast. The model employs the velocity-based equilibrium distribution function, initially proposed for the phase-field-based model by Zu and He [Phys. Rev. E **87**, 043301 (2013)], with a modification necessary to satisfy the kinematic condition at the interface. Different from the existing color-gradient models, the present model allows to specify interface mobility that is independent of the fluid density ratio. Further, we provide a unified framework, which uses the recursive representation of the lattice Boltzmann equation, to derive the governing equations of the system. The emergent color dynamics thus obtained, through an analysis of the segregation operator, is shown to obey the locally conservative Allen-Cahn equation. We use a series of benchmarks, which include a stationary drop, a layered Poiseuille flow, translation of a drop under a forced velocity field, the Rayleigh-Taylor instability, and the capillary intrusion test to demonstrate the model's ability in dealing with complex flow problems.

DOI: 10.1103/PhysRevE.106.045308

I. INTRODUCTION

Lattice Boltzmann (LB) is increasingly becoming the method of choice for the numerical study of multiphase flow problems. Compared to the conventional ones like the volume of fluid [1] or the level set method [2], LB methods offer an advantage over dealing with interface tracking and complex boundaries. For multiphase flow, LB schemes are typically classified as the pseudopotential [3] model, the color-gradient (CG) [4] model, the free-energy [5,6] model, and the phase-field [7] model. Here, we restrict the focus of the present study to the CG model.

One of the first two-phase models for immiscible fluids within lattice Boltzmann framework, known as the chomodynamic or the CG, was proposed by Gunstensen *et al.* [4]. Similar to its predecessor in cellular gas automata [8], the model gets its name by the fact that it uses colored fluid distributions to distinguish between the phases. Apart from the usual collision operation, the CG method is characterized by perturbation and segregation operations. The perturbation operator is used to introduce surface tension while the segregation operator is used to keep the fluids immiscible. Over the past three decades, the CG model has evolved considerably. Reis and Phillips [9] generalized the perturbation operator for the rectangular lattices. In the initial CG models, the segregation operation comprised iteratively maximizing the projection of color flux onto the color gradient. This procedure yields a nearly sharp interface, though it is accompanied by lattice pinning. Later, based on the work of D'Ortona [10], Latva-Kokko and Rothman [11] gave a formulaic prescription of the segregation operator that greatly reduced lattice pinning artifacts. The formulaic prescription also added a length scale to the scheme with a parameter that controlled the interface width. Further, augmented with the wetting boundary conditions and the multiple-relaxation-time (MRT) schemes, the CG model has been employed in a variety of fluid flow situations such as microfluidics [12] and porous media flow [13,14].

Despite the success enjoyed, one of the major challenges with the CG model is to simulate the fluid systems with a large density contrast. Within the weakly compressible LB framework, the fluid pressure is proportional to the density with the squared lattice speed of sound as the prefactor. Consider a planar interface between two immiscible fluids. Due to the planar interface, the surface tension forces are zero. For such a system to remain in equilibrium, the lattice speed of sound must be adjusted. Using this principle, Grunau *et al.* [15] tuned the lattice speed of sound of the individual fluids to maintain the mechanical balance in the presence of density contrast. This approach works well in situations when the fluid velocities are negligible, for example, a stationary drop resting in another fluid. It was later numerically demonstrated [16] that such a construction introduces a momentum discontinuity at the interface for a planar flow between two walls. Huang *et al.* [17] employed the Chapan-Enskog analysis to point out the term, which is proportional to the density gradient and fluid velocity, responsible for such a discontinuity. In this regard, Ba *et al.* [18] made further improvement by constructing an equilibrium distribution based on the third order Hermite expansion of the Maxwellian distribution. The third order lattice velocity moment of the equilibrium distribution exactly cancels the term pointed out by Huang *et al.* [17] for the nondiagonal elements. Using an additional correction to compensate for the diagonal elements, they reported Rayleigh-Taylor instability with a density ratio of 3 and Reynolds number of 2048. A similar approach was used by

---

[*] amol.subhedar@iitb.ac.in

2470-0045/2022/106(4)/045308(16)

Wen *et al.* [19] to extend the model of Ba *et al.* [18] to three dimensions.

The works described above ensure that the individual fluids satisfy the fluid dynamical equations. The mass (density) and momentum sum of the two fluids then also solve the target equations. Another way to approach the problem is to formulate a system where a single fluid satisfies fluid dynamical constraints in both the phases. Along the latter approach, Leclaire *et al.* [20] adopted the equilibrium distribution function of Holdych *et al.* [21], and Che Sidik and Tanabashi [22], which was proposed for a nonideal single component fluid with a density contrast. Later this equilibrium distribution was generalized for rectangular lattices in two and three dimensions [23]. With a judicious choice of the relaxation parameters in the MRT scheme, Saito *et al.* [24,25] employed this model for several complex unsteady problems that include Rayleigh-Taylor instability (density ratio 3, Reynolds number 5120) and liquid jet break-up (density ratio 10, Reynolds number 10^6, Weber number 10^5). Lischuk *et al.* [26] postulated an equation of state in terms of the fluid pressure and the color (phase) field for an incompressible single-phase fluid. With an interfacial term that accounts for both the surface tension and density contrast, they simulated air bubble breaching at density ratio of 10 and Weber number of 3.

Notwithstanding the developments above, the CG model lags the pseudopotential and phase-field-based models in terms of the density ratio and Reynolds number achievable [27–29]. For example, the pseudopotential models are capable of dealing with high-density and high-viscosity ratios at high Weber numbers in three dimensions [30–32]. The phase-field-based models have shown similar capabilities [33–35]. In this work, we present a CG model to address this issue. We modify the velocity-based equilibrium distribution function, first proposed for the single-phase [36] and later for the phase-field-based two-phase model by Zu and He [37]. We introduce a constant term to the color blind fluid populations, which aids in satisfying the kinematic condition at the interface. For the model validation, we simulate a stationary drop and a layered Poiseuille flow with a density ratio of 10^4 and compare the results with the analytical and the finite difference solutions, respectively. Further, we simulate Rayleigh-Taylor instability with a density ratio of 10^3 and Reynolds number of 3×10^3.

The rest of the article is arranged as follows: The CG model and its MRT extension are given in Sec. II. The kinematic properties of the interface tracking are derived and discussed in Sec. III. The model validation through various benchmarks is presented in Sec. IV, while conclusions of the present work are given in Sec. V.

II. CG MODEL WITH VELOCITY EQUILIBRIUM FUNCTION

The CG models typically use colored convention (say blue and red) to identify the two fluids. The total (color-blind) fluid populations are obtained as a sum of the two colored fluid populations,

$$N_i(\mathbf{x}, t) = R_i(\mathbf{x}, t) + B_i(\mathbf{x}, t), \tag{1}$$

where $\mathbf{x}$ is position vector, t is time, and i denotes the lattice direction. Further, R_i and B_i denote the fluid populations in the lattice direction i for the red and the blue phases, respectively. The LB equation for the total (color-blind) fluid populations can be written as

$$\begin{aligned} N_i(\mathbf{x} + \mathbf{c}_i\delta t, t + \delta t) &= N_i(\mathbf{x}, t) + \Omega_i + F_i(\mathbf{x}, t) \\ &= N_i^*(\mathbf{x}, t), \end{aligned} \tag{2}$$

where δt is time step, F_i is force term, N_i^* is total post-collision fluid distribution, and Ω_i is the collision operator. Under the approximation of Bhatnagar-Gross-Crook (BGK) [38] collision operator, N_i^* is given as

$$N_i^* = \left(1 - \frac{1}{\tau}\right)N_i + \frac{1}{\tau}N_i^{\mathrm{eq}} + F_i, \tag{3}$$

where all the quantities are evaluated for the same position and time, τ is the relaxation parameter and N_i^{eq} is the color-blind equilibrium population. Here, we make use of the so-called velocity-based equilibrium distribution function [37] with a modification. In the present work, the color-blind equilibrium population is given as

$$N_i^{\mathrm{eq}} = \begin{cases} \chi_i - (1 - w_i)\frac{p}{c_s^2} - w_i\frac{\mathbf{u}^2}{2c_s^2} & i = 0, \\ \chi_i + w_i\left[\frac{p}{c_s^2} + \frac{\mathbf{c}_i\cdot\mathbf{u}}{c_s^2} + \frac{\mathbf{c}_i\cdot\mathbf{u}}{c_s^4} - \frac{\mathbf{u}^2}{2c_s^2}\right] i \neq 0, \end{cases} \tag{4}$$

where w_i is lattice weight, $\mathbf{c}_i$ is lattice velocity, c_s is lattice speed of sound, $\mathbf{u}$ is fluid velocity, and p is auxillary pressure field. Also $p = \frac{p_h}{\rho}$ with p_h and ρ being the hydrodynamic pressure and fluid density, respectively. For rectangular lattices the lattice speed of sound $c_s = \frac{1}{\sqrt{3}}$ [39]. For the D2Q9 stencil, the lattice velocities $\mathbf{c}$ and lattice weights w_i are given as

$$\mathbf{c} = \begin{pmatrix} 0 & 1 & 0 & -1 & 0 & 1 & -1 & -1 & 1 \\ 0 & 0 & 1 & 0 & -1 & 1 & 1 & -1 & -1 \end{pmatrix}, \tag{5}$$

$$w_i = \begin{cases} \frac{4}{9} & i = 0, \\ \frac{1}{9} & i = 1, 2, 3, 4, \\ \frac{1}{36} & i = 5, 6, 7, 8. \end{cases} \tag{6}$$

The color field φ is used to identify the two phases. We assign the lighter (red) fluid as $\varphi = 0$ and the heavier (blue) fluid $\varphi = 1$. The equilibrium distribution function for the individual fluids is given as

$$\begin{aligned} B_i^{\mathrm{eq}} &= \varphi N_i^{\mathrm{eq}}, \\ R_i^{\mathrm{eq}} &= (1 - \varphi)N_i^{\mathrm{eq}}. \end{aligned} \tag{7}$$

The equilibrium distribution Eq. (4) differs from the one proposed by Zu and He [37] with respect to the addition of the term χ_i. We use χ_i to tune the mobility of the color field. For the D2Q9 lattice, they are given as

$$\chi_i = \begin{cases} \alpha & i = 0, \\ \frac{1-\alpha}{5} & i = 1, 3, 5, 7, \\ \frac{1-\alpha}{20} & i = 2, 4, 6, 8. \end{cases} \tag{8}$$

The free parameter α in Eq. (8) is a positive constant. The zeroth-, first-, second-, and third-order velocity moments of the equilibrium distribution are

$$\sum_i N_i^{\text{eq}} = 1, \quad \sum_i N_i^{\text{eq}} c_{i\alpha} = u_\alpha,$$
$$\sum_i N_i^{\text{eq}} c_{i\alpha} c_{i\beta} = \left[\frac{9(1-\alpha)}{5} + p\right]\delta_{\alpha\beta} + u_\alpha u_\beta,$$
$$\sum_i N_i^{\text{eq}} \mathbf{c}_i \mathbf{c}_i \mathbf{c}_i = (u_\alpha \delta_{\beta\gamma} + u_\beta \delta_{\gamma\alpha} + u_\gamma \delta_{\alpha\beta}) c_{\text{s}}^2. \tag{9}$$

Comparing with the model of Zu and He [37], one finds that the odd lattice velocity moments of the equilibrium distribution [Eq. (4)] remain the same while the even moments differ by constants. The spatial and temporal derivatives of these moments are thus identical to that of Zu and He [37], who have shown that the total fluid satisfies the fluid dynamical equations using the Chapman-Enskog analysis. Here, we use a recursive representation of the LB equation to show the same. This analysis is relegated to the Appendix.

The force term F_i in Eq. (3) is given by [37]

$$F_i = w_i \left(1 - \frac{1}{2\tau}\right) \frac{\mathbf{F}' \cdot \mathbf{c}_i}{c_{\text{s}}^2}, \tag{10}$$

$\mathbf{F}'$ being the total force acting on the fluid. Equation (10) uses the Guo force scheme [40] where the fluid velocity terms are dropped for simplicity. $\mathbf{F}'$ contains both the physical and correction forces, and it is defined as [37]

$$\mathbf{F}' = \mathbf{F}_{\text{visc}} + \mathbf{F}_{\text{p}} + \mathbf{F}_{\text{s}} + \mathbf{F}_{\text{b}}. \tag{11}$$

$\mathbf{F}_{\text{b}}$ and $\mathbf{F}_{\text{s}}$ in Eq. (11) represent the body and surface tension forces. In addition, $\mathbf{F}_{\text{visc}}$ and $\mathbf{F}_{\text{p}}$ are the viscous correction force and pressure correction force, respectively. The expressions for these forces are as follows [37]:

$$\mathbf{F}_{\text{p}} = -p\nabla\rho, \tag{12}$$
$$\mathbf{F}_{\text{visc}} = c_{\text{s}}^2 \delta t \left(\tau - \frac{1}{2}\right)(\nabla\mathbf{u} + \nabla\mathbf{u}^{\text{T}}) \cdot \nabla\rho. \tag{13}$$

The density of the fluid ρ and kinematic viscosity ν are computed by color field φ weighted interpolation of individual fluid properties. In the present model, ρ and ν are computed as

$$\rho = \varphi\rho_{\text{B}} + (1-\varphi)\rho_{\text{R}}, \tag{14}$$
$$\frac{1}{\nu} = \frac{\varphi}{\nu_{\text{B}}} + \frac{1-\varphi}{\nu_{\text{R}}}, \tag{15}$$

where $\rho_{\text{B}}, \rho_{\text{R}}$ ($\nu_{\text{B}}, \nu_{\text{R}}$) are the constant densities (kinematic viscosities) of the blue and red colored fluids, respectively. The relaxation time is found as $\tau = \frac{1}{2} + \frac{\nu}{\delta t c_{\text{s}}^2}$. This relaxation parameter update scheme is simple compared to the more elaborate ones [18,41]. The dynamic viscosity $\mu = \rho\nu$ is then found from the kinematic viscosity and the density.

The color, fluid velocity and auxiliary pressure field are computed as

$$\varphi = \sum_i B_i, \tag{16}$$
$$\mathbf{u} = \sum_i N_i \mathbf{c}_i + \frac{\mathbf{F}'\delta t}{2\rho}, \tag{17}$$
$$p = \frac{1}{1-w_0}\left[-\frac{w_0}{2}\mathbf{u}^2 - (1-\chi_0)c_{\text{s}}^2 + \sum_{i\neq 0} N_i c_{\text{s}}^2\right]. \tag{18}$$

Similar to the model of Zu and He [37], the pressure and velocity terms are implicitly depend on each other in Eq. (17) and Eq. (18). To see it clearly, Eq. (11) and Eq. (12) are used in Eq. (17) to yield

$$\mathbf{u} = \sum_i N_i \mathbf{c}_i + \frac{(\mathbf{F}_{\text{b}} + \mathbf{F}_{\text{visc}} + \mathbf{F}_{\text{s}})}{2\rho}\delta t - \frac{p\nabla\rho}{2\rho}\delta t,$$
$$p = \frac{1}{1-w_0}\left[-\frac{w_0}{2}\mathbf{u}^2 - (1-\chi_0)c_{\text{s}}^2 + \sum_{i\neq 0} N_i c_{\text{s}}^2\right]. \tag{19}$$

We solve Eq. (19) iteratively for a couple of times. Given that the pressure changes slightly over one time step duration, the pressure from the previous time step provides a good initial estimate for the iterative procedure.

A. Perturbation step

Traditionally, CG method incorporates the surface tension effects using a perturbation operator. The force term for this operator can be written as [9,42]

$$F_i^\sigma = A|\nabla\varphi|\left[w_i \frac{(\nabla\varphi \cdot \mathbf{c}_i)^2}{|\nabla\varphi|^2} - B_i\right], \tag{20}$$

where A is proportional to the surface tension and coefficients B_i are lattice specific [9,42]. The scheme given by Eq. (20) removes fluid populations in the tangential direction and adds them to the normal direction while ensuring that the local mass remains unchanged [43]. Other ways to model the surface tension effects include the continuum definition as a distributed force [44]

$$\mathbf{F}_{\text{s}} = \sigma\kappa\delta(\eta)\hat{\mathbf{n}} = -\sigma\nabla \cdot \hat{\mathbf{n}}\nabla\varphi, \tag{21}$$

where σ is the surface tension, κ is the interface curvature, $\delta()$ is a delta distribution, $\hat{\mathbf{n}} = \frac{\nabla\varphi}{|\nabla\varphi|}$ is the unit normal in a direction perpendicular to the interface, η measures distance from the interface and the difference between the extreme color field values is unity. As we show below, the segregation scheme Eqs. (27) and (28) allows to determine the equilibrium shape of the interface profile as $\varphi(\eta) = [1 - \tanh(\frac{2\eta}{W})]/2$. Given the shape of color field profile near equilibrium, it is possible to get a computationally cheaper estimate of local curvature and thus the surface tension force. To see this, first, we express the interface curvature in terms of the color field as

$$\kappa = -\nabla \cdot \left(\frac{\nabla\varphi}{|\nabla\varphi|}\right) = -\frac{1}{|\nabla\varphi|}\left(\nabla^2\varphi - \frac{\nabla\varphi}{|\nabla\varphi|} \cdot \nabla|\nabla\varphi|\right). \tag{22}$$

Equation (22) can be simplified further by noting that $|\nabla\varphi| = \frac{\partial\varphi}{\partial\eta}$. Identifying $\frac{\nabla\varphi}{|\nabla\varphi|} \cdot \nabla$ as the derivative in the normal direction, and using the equilibrium profile for color field [Eq. (47)], Eq. (22) is written as [45]

$$\kappa = -\frac{1}{|\nabla\varphi|}\left[\nabla^2\varphi - \frac{16}{W^2}\varphi(1-\varphi)(1-2\varphi)\right]. \tag{23}$$

Equation (23) expresses the curvature in terms of Laplacian of the color field and a local term, both of which are active only at the interface. This simplification is one of the major reason behind the success of the phase-field models applied to the curvature driven processes as it allows to map the jump boundary conditions at the interface into a second order differential equation [46]. Now choosing $|\nabla\varphi|^2 = (\frac{\partial\varphi}{\partial\eta})^2$ as the delta distribution with an appropriate normalizing factor, and substituting Eq. (23) in Eq. (21), one obtains

$$\mathbf{F}_{\mathrm{s}} = \sigma\left[\frac{48}{W}\varphi(1-\varphi)\left(\frac{1}{2}-\varphi\right) - \frac{3W}{2}\nabla^2\varphi\right]\nabla\varphi. \tag{24}$$

Equation (24) is widely used in phase-field-based two-phase flow models [33,35,47,48], where it is derived from minimization of free energy functional. In the present work, we use Eq. (21) to include the surface tension force.

The computation of surface tension [Eq. (24)] and correction forces [Eqs. (12) and (13)] require the gradient and the Laplacian of the color field. These are approximated as

$$\nabla\varphi = c_{\mathrm{s}}^2\sum_i w_i\varphi(\mathbf{x}+\mathbf{c}_i\delta t)\mathbf{c}_i, \tag{25}$$

$$\nabla^2\varphi = \frac{c_{\mathrm{s}}^2}{2}\sum_i w_i[\varphi(\mathbf{x}+\mathbf{c}_i\delta t)-\varphi(\mathbf{x})]. \tag{26}$$

The truncation errors in the equations above can be shown to be of the order $\mathcal{O}(\nabla^3\varphi)$ and $\mathcal{O}(\nabla^4\varphi)$, respectively [49]. Numerically the unit normal to the interface $\hat{\mathbf{n}}$ is evaluated as $\frac{\nabla\varphi}{|\nabla\varphi|+\epsilon}$, where ϵ [33] is a small positive constant.

B. Segregation step

While the total fluid population takes care of the macroscopic fluid dynamical equations in each of the phases, an additional scheme is needed for interface tracking. Instead of solving an explicit equation for the color field, the CG models use the segregation step for this purpose. The segregation step redistributes the individual fluid populations R_i and B_i near the interface region, and thus preserves the distinction between the phases. Most of the CG models define the color field φ in terms of the normalized density difference between the two phases. Here the color field is independent of the fluid densities, rather the fluid density is computed from the color field variable. In the present work, we use a slightly modified version [50,51] of the segregation operator proposed by Latva-Kokko and Rothman [11]. It is written as

$$B_i^{**} = \varphi N_i^* + 2\frac{\mathbf{c}_i\cdot\hat{\mathbf{n}}}{W}\varphi(1-\varphi)N_i^{\mathrm{eq},\mathbf{u}=\mathbf{0}}, \tag{27}$$

$$R_i^{**} = (1-\varphi)N_i^* - 2\frac{\mathbf{c}_i\cdot\hat{\mathbf{n}}}{W}\varphi(1-\varphi)N_i^{\mathrm{eq},\mathbf{u}=\mathbf{0}}, \tag{28}$$

where B_i^{**} and R_i^{**} are the post-segregation population of the blue and red colored phases, respectively. Further, $N_i^{\mathrm{eq},\mathbf{u}=\mathbf{0}}$ is the equilibrium distribution function evaluated for $\mathbf{u}=0$. Note the omission of $|\mathbf{c}_i|$ in the denominators of second terms in Eqs. (27) and (28) that increases the isotropy of the resulting discrete differential operator [51]. In the spirit of the CG philosophy [43,52], Eqs. (27) and (28) ensure that the individual fluid populations as well as the total fluid populations along each lattice direction are conserved, i.e.,

$$\sum_i R_i^{**} = R_i^*, \sum_i B_i^{**} = \sum_i B_i^*,$$
$$R_i^{**} + B_i^{**} = N_i^*. \tag{29}$$

C. MRT collision operator

Especially for the case of high-viscosity and high-density contrast, MRT collision operator performs better than the BGK collision operator in terms of numerical stability and accuracy. The MRT extension of the present model is

$$N_i^* = N_i - (\mathbf{M}^{-1}\mathbf{S}\mathbf{M})_{ij}\big(N_j - N_j^{\mathrm{eq}}\big) + \left[\mathbf{M}^{-1}\left(\mathbf{I}-\frac{\mathbf{S}}{2}\right)\mathbf{M}\right]_{ij}F_j, \tag{30}$$

where $\mathbf{M}$ is the transformation matrix and $\mathbf{S}$ is the diagonal relaxation matrix. The transformation matrix is given as [33]

$$\mathbf{M} = \begin{pmatrix} 1 & 1 & 1 & 1 & 1 & 1 & 1 & 1 & 1 \\ -4 & -1 & -1 & -1 & -1 & 2 & 2 & 2 & 2 \\ 4 & -2 & -2 & -2 & -2 & 1 & 1 & 1 & 1 \\ 0 & 1 & 0 & -1 & 0 & 1 & -1 & -1 & 1 \\ 0 & -2 & 0 & 2 & 0 & 1 & -1 & -1 & 1 \\ 0 & 0 & 1 & 0 & -1 & 1 & 1 & -1 & -1 \\ 0 & 0 & -2 & 0 & 2 & 1 & 1 & -1 & -1 \\ 0 & 1 & -1 & 1 & -1 & 0 & 0 & 0 & 0 \\ 0 & 0 & 0 & 0 & 0 & 1 & -1 & 1 & -1 \end{pmatrix}. \tag{31}$$

The diagonal relaxation matrix is chosen as [33]

$$\mathbf{S} = \mathrm{diag}(1, 1, 1, 1, 1, 1, s_7, s_8), \tag{32}$$

with $s_7 = s_8 = \frac{1}{\tau}$. A useful way to compute the velocity gradients is to make use of the nonequilibrium part of the fluid populations. We make use of this information to compute the viscous correction force as [33]

$$F_{\mathrm{visc}}^{\alpha} = \left[\sum_i c_{i\alpha}c_{i\beta}(\mathbf{M}^{-1}\mathbf{S}\mathbf{M})_{ij}\big(N_j - N_j^{\mathrm{eq}}\big)\right]\frac{\partial\rho}{\partial x_\beta}. \tag{33}$$

The LB algorithm is complete with the propagation of the fluid populations:

$$N_i(\mathbf{x}+\mathbf{c}_i\delta t, t+\delta t) = N^*(\mathbf{x},t) = N^{**}(\mathbf{x},t), \tag{34}$$

$$R_i(\mathbf{x}+\mathbf{c}_i\delta t, t+\delta t) = R_i^{**}(\mathbf{x},t), \tag{35}$$

$$B_i(\mathbf{x}+\mathbf{c}_i\delta t, t+\delta t) = B_i^{**}(\mathbf{x},t). \tag{36}$$

Finally, the iteration cycle of the algorithm can be summarized as:

(1) The color field is found from the fluid populations and the corresponding spatial derivatives are computed, Eqs. (16), (25), and (26).

(2) The macroscopic force $\mathbf{F}'$, except for the pressure correction force $\mathbf{F}_{\mathrm{p}}$, is evaluated, Eqs. (11), (13), and (24).

(3) The fluid velocity and pressure are evaluated from iterative procedure, Eq. (19). The pressure correction force is evaluated, Eq. (12), and the total force is updated, Eq. (10).

(4) Collision step is carried out for the total fluid populations, Eq. (30).

(5) For the purpose of interface tracking, it is sufficient to consider either of the fluid populations. Segregation step is carried out for the blue fluid, Eq. (27).

(6) The color-blind populations are propagated to the neighbors, Eq. (34).

III. COLOR EVOLUTION

The segregation step is responsible for interface tracking in the CG models. In the interfacial region, this step redistributes the color-blind fluid populations depending upon the phase fractions and thereby introduces equal and opposite forces on the colored phases. These equal and opposite forces, acting in the direction normal to the interface, induce phase separation with a length scale of W. The local mass and momentum of the color-blind fluid remains unchanged during this step. In this section, we investigate the color evolution induced by the segregation step.

The general analysis of the segregation step differs from the single-phase LB equation, in that it couples the colored populations to the color-blind ones on the microscopic level [Eqs. (27) and (28)]. The kinematic condition at the interface requires that the color field moves with the interface velocity, i.e., it is advected with the interface velocity [43,52]. The general purpose of analyzing the segregation step is to ensure that the color field satisfies the kinematic condition and to identify the length scale that separates the fluids. For the latter purpose, steady-state situations have been considered [11,50] while the Chapman-Enskog analysis is used to show that the kinematic condition is satisfied. Recently, Burgin *et al.* [53] and Subhedar *et al.* [51] used the consideration of local density changes to show that the color field indeed satisfies the kinematic condition while identifying the interface width in a single framework.

In this work, we generalize the analysis of the segregation step using the recursive representation of the LB equation [54]. This method expands the fluid populations in a Taylor series around the equilibrium populations to derive the emergent macroscopic equations. The main characteristic of this method is that, unlike the Chapman-Enskog analysis, it recovers the governing macroscopic dynamics in a nonperturbative way [39]. A supplementary order of magnitude analysis is necessary to arrive at the governing macroscopic equations [55]. Lycett-Brown and Luo [56] have demonstrated the utility of this method to identify the truncation errors in the forcing scheme and improve the thermodynamic consistency of the pseudopotential LB model. To keep the analysis simple, we use the BGK collision operator and expand the color-blind populations up to second order in time and space. The consideration of the higher orders in time and space results in Burnett equations [56,57].

We start with the recursive representation of the color-blind fluid populations [54,56]

$$\begin{aligned} N_i = {} & N_i^{\mathrm{eq}} - \tau\delta t D_i N_i^{\mathrm{eq}} + \delta t^2\tau\left(\tau - \frac{1}{2}\right) D_i^2 N_i^{\mathrm{eq}} \\ & + \tau F_i - \tau^2 \delta t D_i F_i, \end{aligned} \tag{37}$$

where $D_i = \partial_t + \mathbf{c}_i \cdot \nabla$ is total derivative in the lattice direction i. Equation (37) expresses the color-blind populations in terms of the corresponding equilibrium populations, which in turn, are known in terms of the macroscopic pressure and fluid velocity. Using Eq. (3) in Eq. (27), we write

$$\begin{aligned} B_i = {} & \left[\left(1 - \frac{1}{\tau}\right)\varphi N_i + \frac{1}{\tau}\varphi N_i^{\mathrm{eq}}\right](\mathbf{x} - \mathbf{c}_i\delta t, t - \delta t) \\ & + \varphi F_i(\mathbf{x} - \mathbf{c}_i\delta t, t - \delta t) + S_i(\mathbf{x} - \mathbf{c}_i\delta t, t - \delta t), \end{aligned} \tag{38}$$

where $S_i = 2\frac{\mathbf{c}_i\cdot\hat{\mathbf{n}}}{W}\varphi(1-\varphi)N_i^{\mathrm{eq},\mathbf{u}=\mathbf{0}}$ is used for brevity. Now Taylor expanding the quantities on the right-hand side around position $\mathbf{x}$ and time t and using Eq. (37) one finds

$$\begin{aligned} B_i = {} & \varphi N_i^{\mathrm{eq}} - \delta t(\tau - 1)\varphi D_i N_i^{\mathrm{eq}} - \delta t D_i\left(\varphi N_i^{\mathrm{eq}}\right) + \frac{\delta t^2}{2} D_i^2\left(\varphi N_i^{\mathrm{eq}}\right) + \delta t^2(\tau - 1) D_i\left(\varphi D_i N_i^{\mathrm{eq}}\right) \\ & + \delta t^2(\tau - 1)\left(\tau - \frac{1}{2}\right)\varphi D_i^2 N_i^{\mathrm{eq}} + \tau\varphi F_i + \delta t(-\tau^2 + \tau)\varphi D_i F_i - \delta t\tau D_i(\varphi F_i) + S_i - \delta t D_i S_i. \end{aligned} \tag{39}$$

To simplify further, the following relations are obtained using Eqs. (4) and (10):

$$\sum_i D_i \varphi N_i^{\mathrm{eq}} = \partial_t\varphi + \nabla \cdot \varphi\mathbf{u}, \tag{40}$$

$$\sum_i D_i^2 \varphi N_i^{\mathrm{eq}} = \partial_t(\partial_t + \nabla\cdot\varphi\mathbf{u}) + \partial_t\nabla\cdot\varphi\mathbf{u} + \nabla\cdot\left\{c_{\mathrm{s}}^2\left[\frac{p}{c_{\mathrm{s}}^2} + \frac{9(1-\alpha)}{5}\right]\nabla\varphi\right\} + \nabla\cdot(\varphi\nabla p + \nabla\cdot\varphi\mathbf{u}\mathbf{u}), \tag{41}$$

$$\sum_i D_i\varphi D_i N_i^{\mathrm{eq}} = \partial_t(\varphi\nabla\cdot\mathbf{u}) + \nabla\cdot(\varphi\partial_t\mathbf{u}) + \nabla\cdot\varphi(\nabla p + \nabla\cdot\mathbf{u}\mathbf{u}), \tag{42}$$

$$\sum_i D_i(\varphi F_i) = \left(1 - \frac{1}{2\tau}\right)\nabla\cdot\frac{\varphi\mathbf{F}'}{\rho}, \tag{43}$$

$$\sum_i D_i S_i = \frac{2c_{\mathrm{s}}^2}{W}\nabla\cdot\varphi(1-\varphi)\hat{\mathbf{n}}, \tag{44}$$

where ∂_t is derivative with respect to time. Summation of Eq. (39) over all the lattice directions and using Eqs. (40)–(44) gives

$$\begin{aligned}\frac{\partial\varphi}{\partial t} + \boldsymbol{\nabla}\cdot\varphi\mathbf{u} = {} & \frac{\delta t c_\mathrm{s}^2}{2}\boldsymbol{\nabla}\cdot\left[\frac{9}{5}(1-\alpha)+\frac{p}{c_\mathrm{s}^2}\right]\left[\nabla\varphi - \frac{4}{W}\varphi(1-\varphi)\hat{\mathbf{n}}\right] + \delta t\left(\tau-\frac{1}{2}\right)\boldsymbol{\nabla}\cdot\varphi\left(\partial_t\mathbf{u}+\boldsymbol{\nabla}\cdot\boldsymbol{\Pi}^{(0)}-\frac{\mathbf{F}'}{\rho}\right)\\ & + \frac{\delta t}{2}\frac{\partial}{\partial t}\left(\frac{\partial\varphi}{\partial t}+\boldsymbol{\nabla}\cdot\varphi\mathbf{u}\right) + \frac{\delta t}{2}\boldsymbol{\nabla}\cdot\mathbf{u}\frac{\partial}{\partial t}\varphi + \frac{\delta t}{2}\boldsymbol{\nabla}\cdot\boldsymbol{\nabla}\varphi\cdot\mathbf{uu}\\ & - (\tau-1)\varphi\boldsymbol{\nabla}\cdot\mathbf{u} + \delta t(\tau-1)\left[\left(\tau-\frac{1}{2}\right)\varphi\nabla\cdot\left(\partial_t\mathbf{u}+\nabla\cdot\boldsymbol{\Pi}^{(0)}-\frac{\mathbf{F}'}{\rho}\right)+\left(\tau-\frac{1}{2}\right)\varphi\partial_t\nabla\cdot\mathbf{u}+\partial_t(\varphi\nabla\cdot\mathbf{u})\right].\end{aligned} \tag{45}$$

Equation (45) governs the color evolution of the blue phase. Given that the terms in the third line on the right-hand side are not in the conservative form, Eq. (45) may give the impression that the color conservation is violated locally. This discrepancy results from the finite truncation of the Taylor expansion of the color field and the color-blind fluid populations. Color conservation is guaranteed with Eqs. (27) and (28) and as we show below, up to the terms considered here, the final equation obeys color conservation. A similar equation can be derived for the red colored phase by transformation $\varphi \to (1-\varphi)$ in Eq. (45). As a necessary condition, Eq. (45), when evaluated in the bulk phase ($\varphi = 1$), reverts to the single-phase continuity equation, Eq. (A10).

The first term on the right-hand side of Eq. (45) is responsible for keeping the interface of fixed shape and width, while the other terms generate additional coupling between the color and fluid velocity. The presence of the terms in the second and the third line can be understood as purely a consequence of the segregation operator, which divides the color-blind populations among the two phases based on their phase fractions.

For the case of equal densities, the correction forces due to the density gradient at the interface are absent, and $\mathbf{F}'$ in Eq. (45) represents the physical forces alone. A comparison of the color evolution Eq. (45) with the one derived by Subhedar *et al.* [51] for the equal density case reveals the terms have second derivative with respect to time. Further, the effect of the nonequilibrium part of the color-blind fluid populations on the color evolution can be separated by substituting $N_i \approx N_i^{\mathrm{eq}}$ (or $\tau = 1$) in Eq. (38). In this case, the third line on the right-hand side of Eq. (45) vanishes. The remaining terms are in agreement with the work of Burgin *et al.* [53], where a uniform flow field ($N_i \approx N_i^{\mathrm{eq}}$) was assumed to recover color dynamics. Equation (45) extends these studies by taking into account a general velocity field (via consideration of the nonequilibrium color-blind fluid populations) and the density contrast.

Next, we estimate the order of magnitude of the terms other than the first one on the right-hand side of Eq. (45). We use Eq. (A12), Eq. (A13), and Eq. (45) itself in Eq. (45) to obtain

$$\begin{aligned}\frac{\partial\varphi}{\partial t} + \boldsymbol{\nabla}\cdot\varphi\mathbf{u} = {} & \boldsymbol{\nabla}\cdot M\left[\nabla\varphi - \frac{4}{W}\varphi(1-\varphi)\hat{\mathbf{n}}\right]\\ & + \mathcal{O}(\delta t^2 + \mathrm{Ma}^2\delta t),\end{aligned} \tag{46}$$

where $M = \frac{c_\mathrm{s}^2\delta t}{2}[\frac{9(1-\alpha)}{5} + \frac{p}{c_\mathrm{s}^2}]$ is the mobility of the interface. The equation is, in fact, a locally conservative Allen-Cahn (AC) equation with a source term. The models that explicitly solve AC or Cahn-Hilliard equation for interface tracking provide feedback to the color field only through the fluid velocity in the advection term. Equation (46) thus differs slightly from them in that an additional feedback, although a weak one of the order $\delta t^2 + \mathrm{Ma}^2\delta t$, is given to the color field. The equilibrium solution of Eq. (46), with fluid velocity and temporal derivative of the color field being zero, can be easily verified as

$$\varphi(\eta) = \frac{1}{2}\left[1 \pm \tanh\left(\frac{2\eta}{W}\right)\right], \tag{47}$$

where η measures signed distance from the interface.

The interface mobility M determines the relaxation rate of the interface. Ideally, the interface mobility should be small enough such that the interface does not move under the influence of artificial forces that tend to restore radial symmetry [51]. For this reason, we choose the initial uniform pressure of the system as $p = 0$. This choice does not affect the macroscopic governing equations as the hydrodynamic pressure of the system is determined only within a constant. The fluctuations of the hydrodynamic pressure p_h are of the order of Ma^2 for incompressible fluids [58,59]. Therefore, the fluctuations $\delta p = \frac{\delta p_h}{\rho}$ are also of the order Ma^2 and the interface mobility changes only slightly during the simulations.

IV. NUMERICAL RESULTS

In this section, we test the model with various steady-state and transient flow simulations. In all of the simulations p, and therefore p_h, is set to zero initially. The interface mobility M reported corresponds to its constant part neglecting the pressure fluctuations, i.e., $M = \frac{3(1-\alpha)}{10}$. All the simulation quantities in this section are given in the lattice units.

A. Stationary drop

The stationary drop test allows to judge the accuracy of surface tension forces and the inherent (without contact with the solid surface) spurious currents present in the model. Spurious currents may compromise the accuracy of the overall simulation, for example, when applied to flow in a porous medium [60]. Initially, a fluid drop, with a higher density than the surrounding fluid, is placed at the center of the system. The system consists of a square domain of size $L \times L$, with $L = 100$ and the initial radius of the drop $R_0 = 25$. Periodic boundary conditions are applied on all the boundaries. The kinematic viscosities of both the fluid are kept the same with $\nu_\mathrm{B} = \nu_\mathrm{R} = 0.1667$, the density ratio is chosen as $\frac{\rho_\mathrm{B}}{\rho_\mathrm{R}} = 10^4$

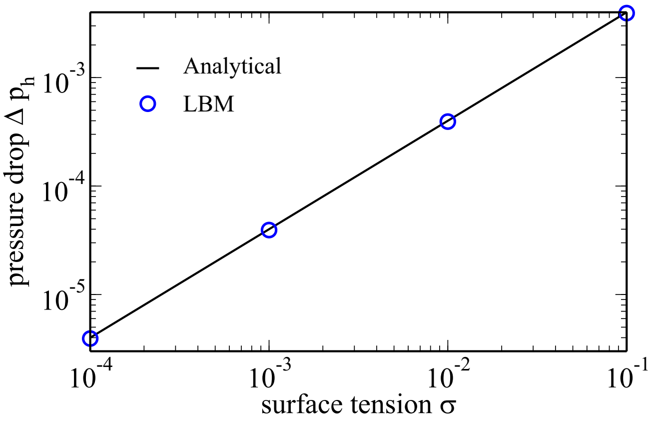

FIG. 1. A comparison of the analytical pressure drop, found from Eq. (49), with that evaluated from the simulations. The initial radius of the drop $R_0 = 25$, the density ratio $\frac{\rho_\mathrm{B}}{\rho_\mathrm{R}} = 10^4$, the interface width $W = 5$, and the viscosity ratio $\frac{\mu_\mathrm{B}}{\mu_R} = 10^4$ are kept constant.

and the interface mobility is $M = 0.01$. The system is initialized with a zero fluid velocity everywhere and with the color field as follows:

$$\varphi(\mathbf{r}) = \frac{1}{2}\left\{1 - \tanh\left[\frac{2(r-R_0)}{W}\right]\right\}, \tag{48}$$

where r is the distance from the origin and the interface width $W = 5$. Due to the surface tension forces, a pressure difference inside and outside is developed over time. When the viscous dissipative forces are settled in, the pressure difference (in two dimensions) is given by

$$\Delta p_h = \frac{\sigma}{R}, \tag{49}$$

where Δp_h is measured as the difference of pressure at the center and at the boundary and R is the steady-state radius. R is determined from a linear interpolation by transversing along the line $y = \frac{L}{2}$ to locate the point $\varphi = \frac{1}{2}$. To test Eq. (49), the surface tension is varied while keeping the radius of the drop constant. Figure 1 compares the pressure drop measured in the simulations and as predicted by Eq. (49). The pressure drop measured in the simulations matches closely with the analytical ones and the maximum relative error of 1.8% occurs at the surface tension $\sigma = 0.1$ for these data points. Further, it is instructive to compare the initial and the steady-state color field profiles along a line passing through the center of the drop $(y = \frac{L}{2})$ for different density ratios. For this purpose, the interface width $W = 5$, the initial drop radius $R_0 = 25$, the surface tension $\sigma = 10^{-2}$ and the viscosity ratio $\frac{\nu_\mathrm{B}}{\nu_\mathrm{R}} = 1$ are kept constant. Figure 2 shows such a comparison. Due to the incompressible nature of the color-blind fluid, the initial (analytical) and the steady-state interface profile almost coincide with each other. This match suggests a minimum numerical dispersion that is independent of the density ratio.

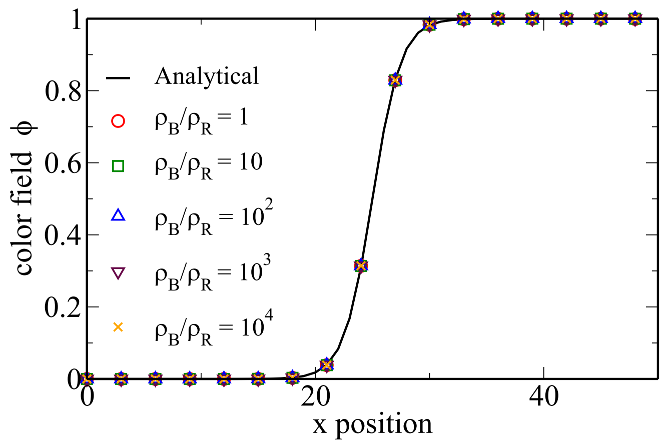

FIG. 2. A comparison of the steady-state color field profiles along a line passing through the center $(y = \frac{L}{2})$ for different density ratios with the initial (analytical) solution. Surface tension $\sigma = 10^{-2}$ is kept constant for all the cases. The steady-state color fields match excellently to the analytical ones for all the density ratios.

Spurious currents are the undesired velocity field near the interfacial region that result from the distributed surface tension forces [61]. Figure 3 shows the steady-state spurious currents for the same geometry and physical parameters ($\frac{\rho_\mathrm{B}}{\rho_\mathrm{R}} = 10^4$, $\frac{\nu_\mathrm{B}}{\nu_\mathrm{R}} = 1$) with the surface tension $\sigma = 10^{-2}$. Due to the underlying rectangular lattice, the spurious currents exhibit an eightfold symmetry with an intensified activity near the interface. The corresponding contour of interface $(\varphi = \frac{1}{2})$ is also shown in the figure. The maximum magnitude of the velocity is $|\mathbf{u}_\mathrm{max}| = 1.64 \times 10^{-9}$ in this case. Next, we look at the effect of density ratio on the Laplace pressure error and the activity of spurious currents. The geometry of the system is kept same, and other parameters are: $\sigma = 0.01$, $\nu_\mathrm{B} = 0.01$, $\nu_\mathrm{R} = 0.1$, $W = 5$, and $M = 0.01$. The relative error in the

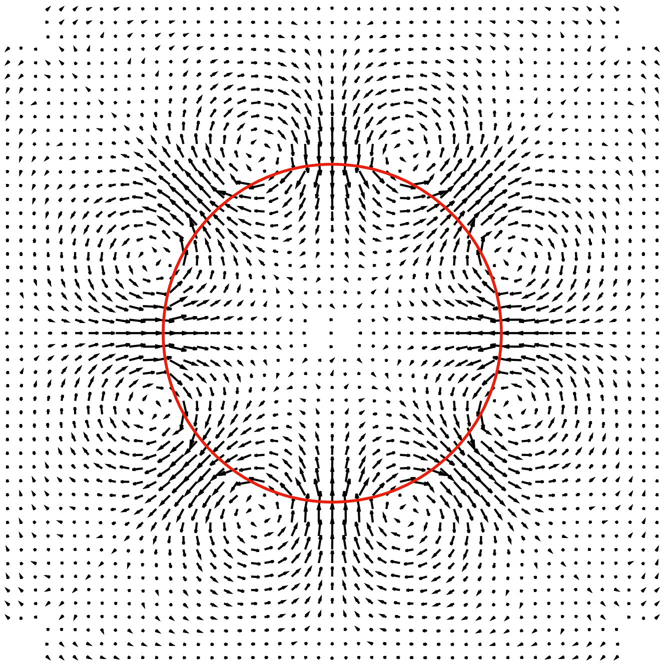

FIG. 3. Spurious currents are shown in black solid arrow and the interface profile with a red solid line, at the steady state. The system size is $L \times L$ with $L = 100$ and the initial radius of the drop $R_0 = 25$. The density and dynamic viscosity ratios are both equal to 10^4 and the surface tension $\sigma = 10^{-2}$. The magnitude of the maximum spurious velocity at the steady state is $|\mathbf{u}_\mathrm{max}| = 1.64 \times 10^{-9}$.

TABLE I. Relative pressure error and spurious currents magnitude.

	Present work				Ref. model [18]	
	$M = 0.01$		$M = 0.26$			
ρ^*	Δp_h^E	$\lvert\mathbf{u}_{\max}\rvert$	Δp_h^E	$\lvert\mathbf{u}_{\max}\rvert$	Δp_h^E	$\lvert\mathbf{u}_{\max}\rvert$
10	1.7	1.44×10^{-7}	1.6	7.56×10^{-7}	0.28	9.67×10^{-7}
10^2	1.35	2.08×10^{-8}	1.34	2.37×10^{-7}	0.37	5.71×10^{-6}
10^3	1.07	1.21×10^{-8}	1.07	4.35×10^{-8}	4.21	1.27×10^{-5}

Laplace pressure is quantified as follows:

$$\Delta p_h^E = \left| \frac{\Delta p_h - \Delta ps_h}{\Delta p_h} \right| \times 100, \tag{50}$$

where Δp_h and Δps_h are the analytically predicted and the simulated pressure differences at steady state, respectively. Table I compares Δp_h^E and $|\mathbf{u}_{\max}|$ values with the model of Ba *et al.* (reference model) [18] for different density ratios. Relative to the present model, the reference model [18] has a lower Laplace pressure error except for high-density ratio $\mathcal{O}(1000)$. However, the present model produces lower spurious currents magnitude $|\mathbf{u}_{\max}|$ for all the density ratios compared to the reference model [18]. Table I also shows the corresponding quantities for interface mobility $M = 0.26$. The Laplace pressure error in the present work is nearly independent of the interface mobility. The spurious currents magnitude $|\mathbf{u}_{\max}|$, however, increases with the interface mobility. Zu and He [37] made similar observations, where they employed Cahn-Hilliard equation for an explicit solution of the phase-field equation.

B. Layered Poiseuille flow

The system geometry consists of a channel with length $L = 100$, separated by two parallel walls. Initially, the heavy (blue) fluid occupies the region $x < \frac{L}{2}$ while the rest is filled with the light (red) one. Gravity force $(0, \rho g_y)$, applied in the y direction, is used to drive the flow. Periodic boundary condition is applied in the direction of the length of the wall while the halfway bounce-back rule [62] is used to impose the no-slip boundary condition at the wall. Other simulation parameters are: surface tension $\sigma = 0$, interface width $W = 4$, and interface mobility $M = 1.6 \times 10^{-2}$.

The system is initiated with zero velocity everywhere. Under the applied pressure gradient in the form of gravity, the fluid velocity is developed while forming a diffuse interface. The steady-state equation for the fluid velocity component u_y can be written as

$$0 = \frac{\partial}{\partial x}\left[\rho(x)\nu(x)\frac{\partial u_y}{\partial x}\right] + \rho(x)g_y. \tag{51}$$

The analytical solution of the equation above can be found by representing the kinematic viscosity and the density as a step function across the interface. Such a solution, however, does not account for the inherent diffuse interface nature of the model. For this reason, we solve Eq. (51) with a finite difference (FD) scheme for which the kinematic viscosity and density are interpolated with Eqs. (14) and (15), respectively. First, we consider the case of unit density ratio and variable kinematic viscosity ratio. The kinematic viscosity of the red fluid is fixed at $\nu_{\mathrm{R}} = 0.01$ while that of the blue fluid is varied to obtain different $\frac{\nu_{\mathrm{B}}}{\nu_{\mathrm{R}}}$ ratios. The scaled steady-state velocity profiles obtained with the present model, the reference model [18] and the FD solutions are shown in Fig. 4. For all the kinematic viscosity ratios considered, the LBM solutions are well in agreement with the FD solution. Next, with a constant dynamic viscosity ratio $\frac{\mu_{\mathrm{B}}}{\mu_{\mathrm{R}}} = 100$, four different test cases are considered where the density ratio is varied from 10 to 10^4. A comparison of solutions with the FD scheme, the present model, and the reference model is shown in Fig. 5. Solutions obtained with these numerical methods are in a good agreement, although a slight difference is observed for higher density ratios. At increasing density ratios, the discretization errors due to correction forces [Eqs. (12) and (13)] continue to increase. Thus, the spatial resolution of the interface and the system size needs to adjusted to accommodate these discretization errors. In this regard, the Cahn number $\mathrm{Cn} = \frac{W}{L}$ indicates the influence of the diffuse interface with $\mathrm{Cn} \rightarrow 0$ corresponding to the sharp interface limit. To quantify the difference between the FD and LBM solutions, E_2 is defined as the normalized root mean squared error between the two solutions:

$$E_2 = \sqrt{\frac{\sum_x \left(u_y - u_y^{\mathrm{FD}}\right)^2}{\sum_x \left(u_y^{\mathrm{FD}}\right)^2}}. \tag{52}$$

Choosing density ratio $\frac{\rho_{\mathrm{B}}}{\rho_{\mathrm{R}}} = 1000$ and viscosity ratio $\frac{\mu_{\mathrm{B}}}{\mu_{\mathrm{R}}} = 100$, E_2 is evaluated for different channel lengths at a fixed Cahn number $\mathrm{Cn} = 7 \times 10^{-2}$. Figure 6 shows that the error E_2 continues to decrease with channel length L, indicating that sufficient resolution of the system is necessary to deal with high-density ratios to achieve a given accuracy.

C. Interface kinetics

The previous two benchmarks correspond to the steady state of the system. A numerical model solving $\frac{\partial \varphi}{\partial t} + \nabla \cdot (k\varphi \mathbf{u}) = 0$ for an arbitrary k as would pass these tests as they do not involve fluid flow in the direction of the density gradient. In this section, we verify that the fluid velocity indeed advects the color field and that a stable interface is maintained via the segregation step is, in fact, an AC equation. For the former purpose, we consider a circular drop of radius of $R_0 = 25$, translating through a square domain of size $L \times L$ with $L = 100$. The drop is subjected to a forced velocity field $\mathbf{u}_{\mathrm{forced}} = (U, U)$ in the diagonal direction of the system. At each time step, the equilibrium color-blind fluid distribution is populated with the forced velocity $\mathbf{u}_{\mathrm{forced}}$. Other simulation parameters are: $\frac{\rho_{\mathrm{B}}}{\rho_{\mathrm{R}}} = \frac{\mu_{\mathrm{B}}}{\mu_{\mathrm{R}}} = 5$, $\sigma = 0$, $M = 6.67 \times 10^{-3}$, $W = 5$. Given the linearly symmetric nature of the imposed velocity field, the interface advects along the diagonal of the system and returns to the initial position in time $T = \frac{L}{U}$. The interface Péclet number here is defined as $\mathrm{P\acute{e}} = \frac{UW}{M}$ that indicates the dominance of the advection process over the interface stabilizing numerical diffusion process. In the present setting $\mathrm{P\acute{e}} = 5$.

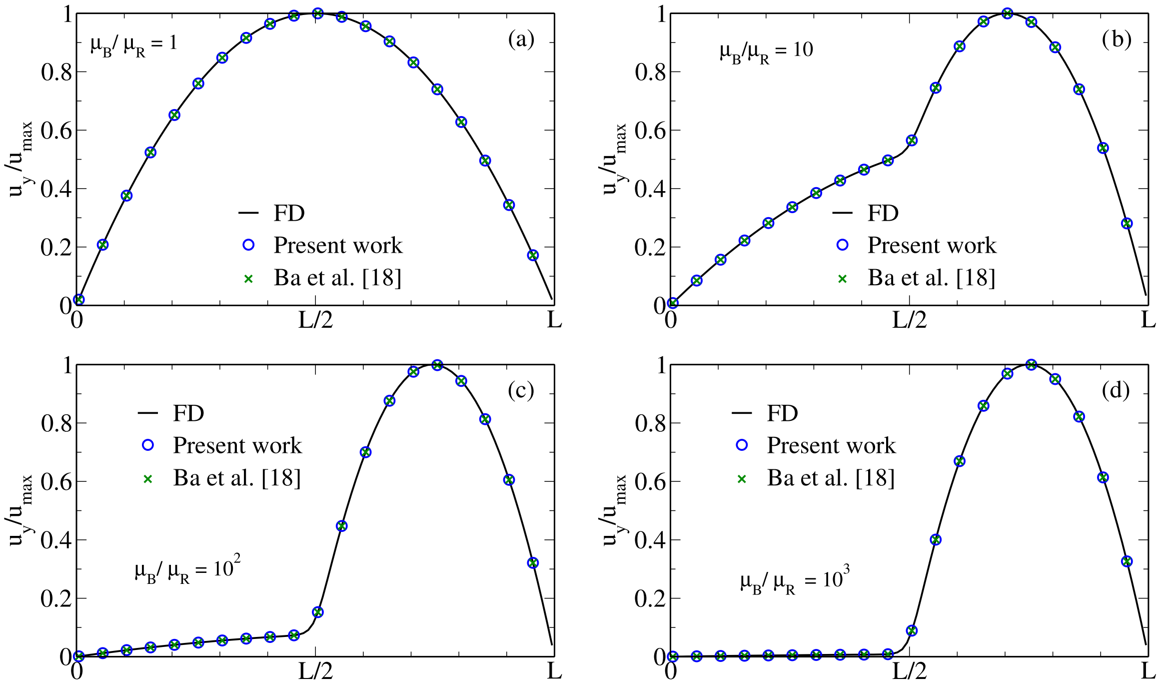

FIG. 4. Comparison of the numerical solutions obtained from the present method (LBM), the reference model [18] and the finite difference scheme by solving Eq. (51). The kinematic viscosity of the red fluid is fixed at $\nu_R = 0.01$. The density ratio $\frac{\rho_B}{\rho_R} = 1$ is kept constant for all of the cases. The dynamic viscosity ratio $\frac{\mu_B}{\mu_R}$ is (a) 1, (b) 10, (c) 10^2, and (d) 10^3.

Figure 7 shows the interface contour after one cycle obtained using the present and the reference model [18]. The interface contour of the present work coincides well with the initial interface contour. The close match between the two contours confirms that the color field indeed follows an advection equation. Also, the interface profile of the refer-

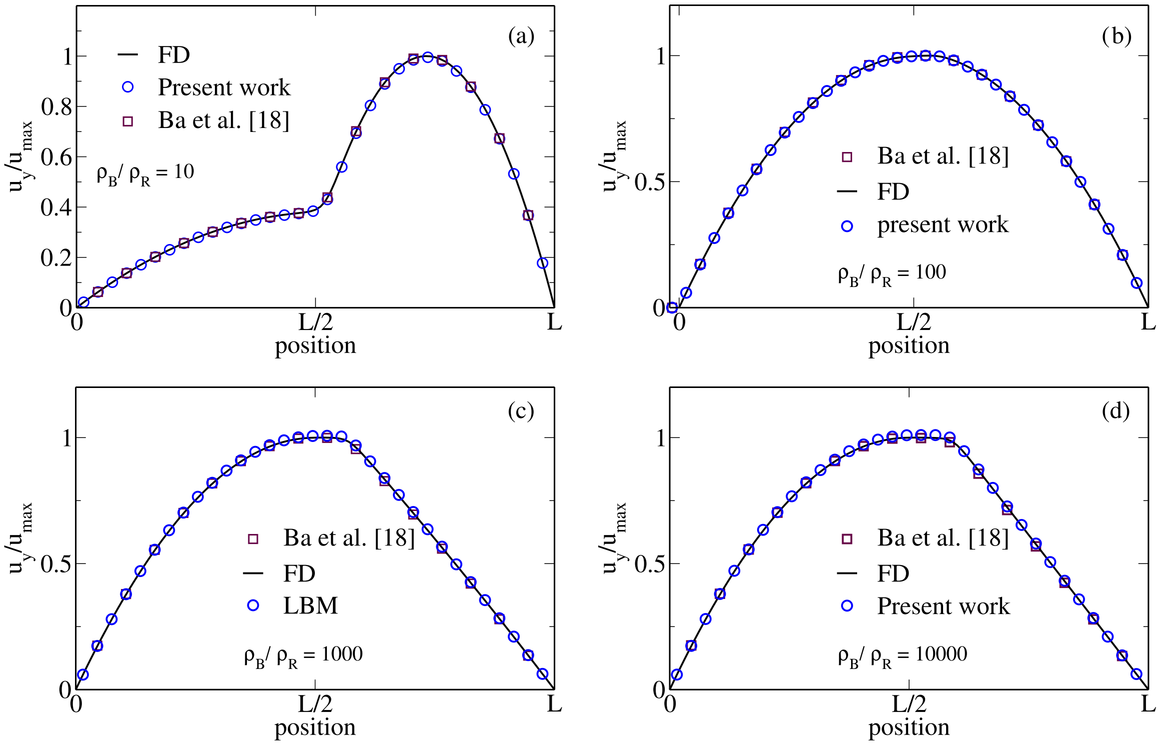

FIG. 5. Comparison of the numerical solutions obtained from the present work (LBM), reference model [18] and the finite difference scheme by solving Eq. (51). The kinematic viscosity of the lighter red fluid is fixed at $\nu_R = 0.1667$. The viscosity ratio $\frac{\mu_B}{\mu_R} = 100$ is kept constant for all of the cases. The density ratio $\frac{\rho_B}{\rho_R}$ is (a) 10, (b) 10^2, (c) 10^3, and (d) 10^4.

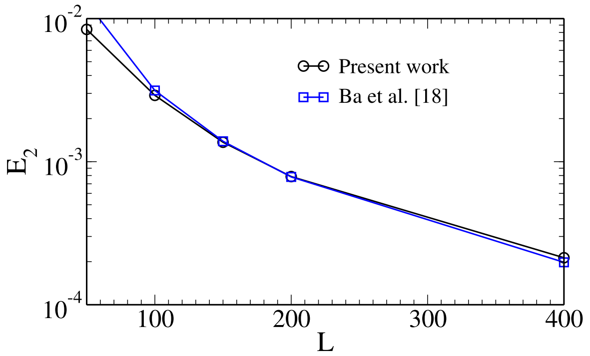

FIG. 6. Plot of the normalized root-mean-squared error E_2 [Eq. (52)] as a function of channel length L. The density ratio $\frac{\rho_B}{\rho_R} = 10^3$, viscosity ratio $\frac{\mu_B}{\mu_R} = 10^2$, and Cahn number $\mathrm{Cn} = 7 \times 10^{-2}$ are fixed. For both, the present (in black color) and the reference model [18] (in blue color), E_2 behaves similarly and decreases with the channel length L.

ence model [18] deviates slightly from the initial interface contour indicating that the interfacial correction terms are not sufficient to maintain the interface shape. As a further test, the density ratio is increased to 10^3 while keeping the other parameters the same. The interface profile after one cycle still coincides well with the initial one as shown in Fig. 8.

To test the AC nature of the color segregation step, we study the evolution of a square shaped fluid body at negligible surface tension. The heavier (blue) fluid of size $d \times d$ is placed at the center of the system filled with the lighter (red) one. The system size is $L \times L$ with periodic boundary conditions applied on all the boundaries. Besides, the system starts with a zero fluid velocity everywhere, and no external force acts on the system. Given that the surface tension is zero, the fluid velocity remains zero at all the time. Other parameters of the system are $\frac{\rho_B}{\rho_R} = \frac{\mu_B}{\mu_R} = 100$, $W = 4$, and $M = 0.1667$.

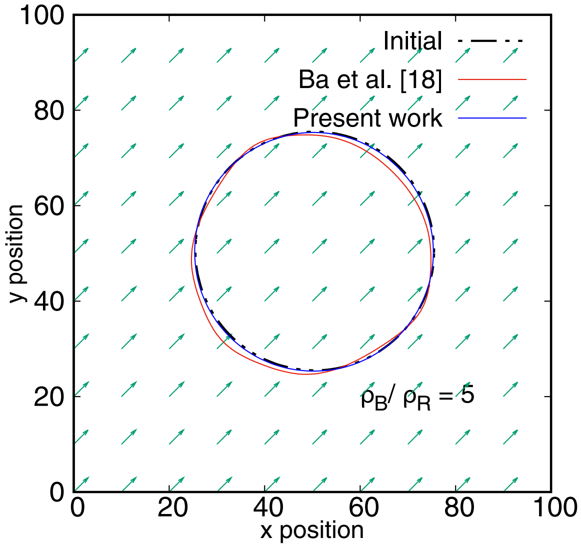

FIG. 7. A comparison of the interface profile at the start of the simulation (black dashed line) with present method (blue solid line) and the reference model [18] after time $t = T$. The system size is $L \times L = 100 \times 100$, density ratio is 5 and the radius of initial profile is $R_0 = 25$. The interface is subjected to a forced advection along a line parallel to the diagonal of the square system (shown with green arrows).

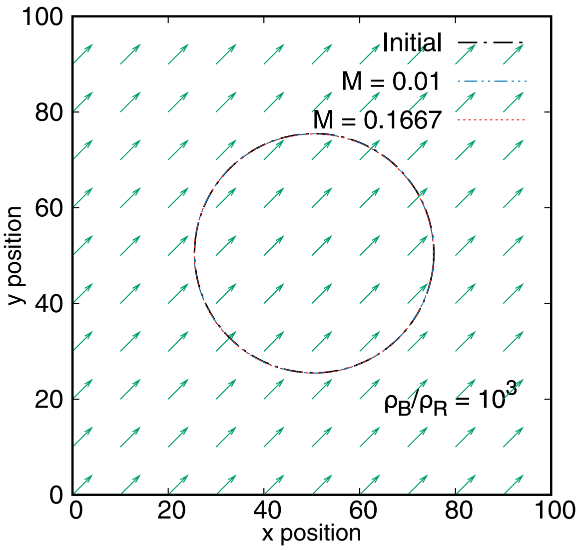

FIG. 8. A comparison of the interface profile at the start of the simulation (black dashed line) and the one after time $t = T$ for two interface mobilities: $M = 0.01$, (blue dashed line) and $M = 0.1667$ (red dotted line). The system size is $L \times L = 100 \times 100$, density ratio is 10^3 and the radius of initial profile is $R_0 = 25$. The interface is subjected to a forced advection along a line parallel to the diagonal of the square system (shown with green arrows). For both the interface mobilities, the interface profile after one cycle matches well with the initial one.

Under this setting, and in the sharp interface limit, the fluid-fluid interface now should remain stationary for an indefinite amount of time. Within the present diffuse interface approach, however, the color evolution implicitly proceeds with Eq. (46). Thus, any change in the interface shape will be due to the segregation step. The evolution continues until a radially symmetric interface shape is reached, in this case, a circle [51]. The timescale of the evolution is given by $t_d = \frac{d^2}{M}$.

Figure 9 shows the evolution of the interface profile at different times. Along with it, the solution of the standalone AC equation with the same initial conditions and mobility $M = 0.1667$ is also shown. This solution is obtained by using a scheme outlined by Geier *et al.* [63]. Both of these solutions match well throughout until a circular shape is reached. The artificial interface motion due to the diffuse interface modeling can be minimized by lowering the interface mobility M. To see this, we set the interface mobility $M = 1.6 \times 10^{-2}$ and repeat the procedure above. Again, the explicit solution of the AC equation matches well with the CG scheme, and the artificial motion of the interface is reduced by lowering the interface mobility. For a general fluid dynamical problem, the numerical diffusivity time t_d should be sufficiently large compared to the physical advective timescale $t_a = \frac{d}{U}$ with U being the characteristic fluid velocity. Typically, the advective timescale is specified by the system and the interface mobility should be adjusted to ensure that the interface moves due to

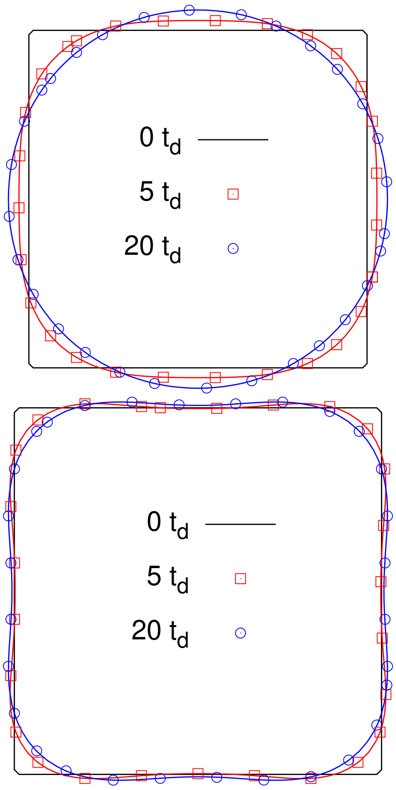

FIG. 9. Evolution of a square shaped fluid body at vanishing surface tension. The initial position of the interface is shown in black solid line. Top: The interface mobility is $M = 0.1667$. The CG solution at time $5t_d$ and $20t_d$ ($t_d = \frac{d^2}{M}$) are shown with points and the corresponding solution of the explicit AC equation are shown with solid lines. The two solutions overlap each other and a nearly circular shape is reached at $t = 20t_d$. Bottom: With interface mobility $M = 1.67 \times 10^{-2}$, the interface evolution towards a circular shape is slowed down when compared at the same physical time.

the fluid velocity alone. Arbitrarily small interface mobility M, however, decreases the importance of a diffuse interface maintaining mechanism and creates numerical instability.

Unlike the present model, for most of the existing CG models, the interface mobility depends upon the density ratio [53]. Here, we tuned the interface mobility by adjusting the parameter α in the lattice coefficients χ_i. Although α can be chosen independently of the fluid densities, this approach is not without its limitations. Deviation of α from $\frac{4}{9}$ results in loss of fourth order isotropy of the lattice coefficients χ_i [64]. This loss results in the discretization errors that prevent the segregation step to achieve mobility as low as in the explicit solution of the AC equation ($M \approx 10^{-3}$) [33].

D. Rayleigh-Taylor instability

A heavy fluid lying on top of another lighter one and separated by a planar interface may form a system in an unstable equilibrium under the presence of gravity. A small perturbation in the interface shape separating the fluid initiates the interplay of surface tension, viscous and inertial forces that may result in penetration of the heavier fluid inside the lighter one. This phenomenon, known as the Rayleigh-Taylor instability, provides a test to validate the model's ability to handle complex physics [18,37,65,66].

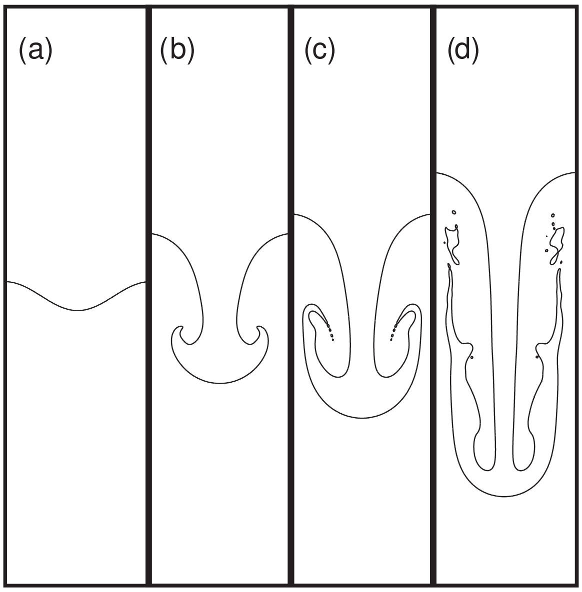

FIG. 10. The Rayleigh-Taylor instability at Re = 3000, capillary number Ca = 0.24, and Atwood number At = 0.5. The interface position is shown for time $t =$ (a) 0, (b) $1.5t_0$, (c) $2t_0$, and (d) $3t_0$. The system size is $L \times 4L$ with $L = 256$.

The system consists of a rectangular domain with the size $L \times 4L$ and $L = 256$. The interface between the two phases is given as

$$y(x) = 2L + \frac{L}{10}\cos\left(\frac{2\pi x}{L}\right), \tag{53}$$

where the second term corresponds to the perturbation applied to the flat interface. The heavy (blue) fluid occupies the top part, and the light (red) fluid occupies the bottom part of the system. Periodic boundary conditions are applied on the lateral boundary ($x = 0$ and $x = L$) and the halfway bounce-back rule [62] is applied at the top and bottom boundary. The density ratio is $\frac{\rho_B}{\rho_R} = 3$ and viscosity ratio is $\frac{\nu_B}{\nu_R} = 1$. Some important dimensionless numbers of the system are Reynolds number Re, Atwood number At, and capillary number Ca. They are defined as

$$\mathrm{Re} = \frac{LU}{\nu_B}, \tag{54}$$

$$\mathrm{At} = \frac{\rho_B - \rho_R}{\rho_B + \rho_R}, \tag{55}$$

$$\mathrm{Ca} = \frac{\mu_B U}{\sigma}, \tag{56}$$

where characteristic fluid velocity $U = \sqrt{Lg}$. The component of the gravity acting in the y direction is chosen as $g_y = g = -2.0 \times 10^{-6}$ and surface tension is chosen as $\sigma = 2.45 \times 10^{-3}$. These choice of parameters corresponds to At = 0.5, Re = 3000, and Ca = 0.26. In addition, the timescale of the process is given as $t_0 = \sqrt{\frac{L}{g\mathrm{At}}}$. Auxiliary parameters of the system are selected as $W = 4$ and $M = 1.67 \times 10^{-2}$.

Figure 10 shows the evolution of the interface at various times. The heavy fluid near the center comes down and

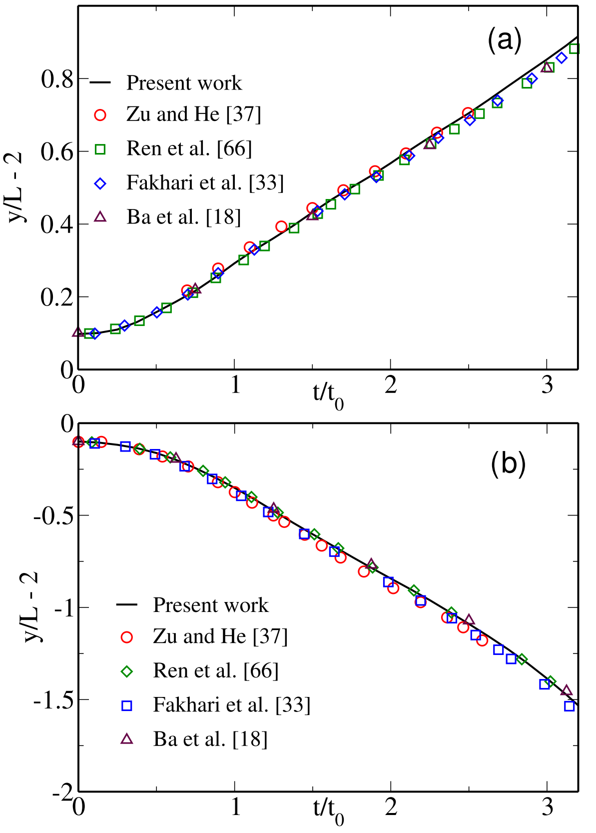

FIG. 11. Scaled position of the (a) bubble position ($x = 0$) and (b) spike ($x = L/2$) versus scaled time for the case of At = 0.5, Re = 3000, and Ca = 0.26, compared with other numerical works [18,33,37,66].

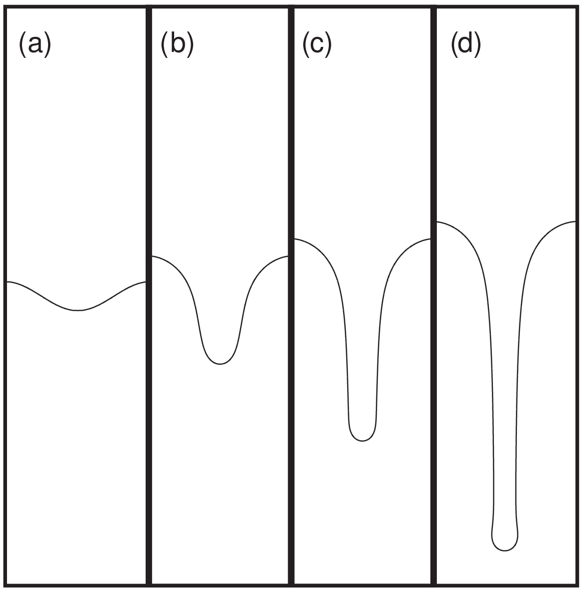

FIG. 12. The Rayleigh-Taylor instability at Reynolds number Re = 3000, Atwood number At = 0.998, capillary number Ca = 0.44. The interface position is shown for time t = (a) 0, (b) t_0, (c) $1.5t_0$, and (d) $2t_0$.

gradually rolls up. Around time $t = 3t_0$, a breakup of smaller droplets is seen. For a quantitative validation, we compare the location of the spike ($x = L/2$) and the bubble front ($x = 0$) with other numerical works. Figure 11 shows that the location of both the spike and bubble front are in good agreement with previous works.

To simulate systems with a high-density ratio, the initial conditions require careful consideration. When the interface is initialized with a sharp interface, the force terms dependent upon the color field give rise to unphysical fluid velocities. The fluid velocity then may quickly reach lattice speed of sound c_s that may result in a numerical instability, especially at high-density ratios and Reynolds number. Therefore, we find it necessary to ensure that the interface is stabilized and reaches the given interface width before the fluid dynamical effects are set in motion. For the systems with radial symmetry, the initial interface profile can be specified in terms of its equilibrium solution. For more complex geometries, we propose the following scheme for a smooth initialization. First, the segregation for either of the fluid (say blue) is solved using total equilibrium populations with zero fluid velocity and zero pressure, i.e., $\mathbf{u} = 0, p = 0$. The blue color fluid populations are then propagated [Eq. (36)] and finally the color field is found from the sum of the fluid populations Eq. (16). This procedure is repeated for a number of steps, roughly $3t_d$, where $t_d = \frac{W^2}{M}$ is the momentum diffusion time of the interface. If the relaxation process is carried out for a longer time, the interface shape may deviate from the target one, due to the artificial forces that tend to restore the radial symmetry [51]. It is noteworthy that a smooth initialization technique for the CG models that employ momentum-based equilibrium distribution function is outlined by Leclaire *et al.* [67].

The typical density ratio employed in the CG models for the Rayleigh-Taylor instability simulation is $\frac{\rho_{\rm B}}{\rho_{\rm R}} = 10$ [18,24]. Using the scheme outlined above, we simulate a system with Re = 3000 and density ratio $\frac{\rho_{\rm B}}{\rho_{\rm R}} = 1000$. Here, the Atwood number At = 0.998 and the capillary number Ca = 0.44. Figure 12 shows the evolution of the interface at times $t = 0, t_0, 1.5t_0$, and $2t_0$. Due to the much higher density contrast, the heavy fluid continues to move downwards without forming a roll up. The positions of the bubble ($x = 0$) and spike ($x = L/2$) are shown in Fig. 13 which are in good agreement with the work of Dinesh Kumar *et al.* [68].

E. Capillary displacement

The multiphase flow in porous media is controlled by the pore geometry, dynamic viscosity ratio, and the wetting tendencies of the fluids. It is usually characterized by low Reynolds and Capillary numbers, where the pore radius sets the length scale of the flow. The capillary intrusion test [23,69,70] provides a good benchmark to mimic the two-phase flow in porous media at relatively low capillary numbers.

A typical simulation domain is shown in Fig. 14. The rectangular domain has dimensions of $N_x \times N_y = 800 \times 35$. A solid tube of width $H = 20$ and extending from $x = 200$ to $x = 600$ in length is placed inside the system. The red fluid occupies the domain from $x = 240$ to $x = 750$ while the

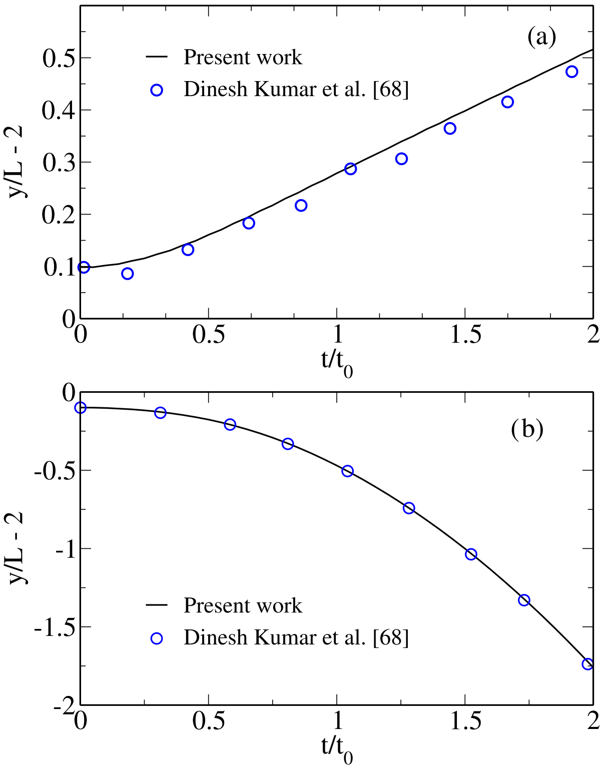

FIG. 13. Scaled position of the (a) bubble position ($x = 0$) and (b) spike position ($x = L/2$) versus scaled time t/t_0 for the case of Atwood number At $= 0.998$, Reynolds number Re $= 3000$, and capillary number Ca $= 0.44$. The bubble and spike positions agree well with the work of Dinesh Kumar *et al.* [68].

blue fluid occupies the rest of the domain. Periodic boundary conditions are applied in all directions. Other parameters are $M = 0.1667$, $\sigma = 0.01$, and $W = 5$. The wetting contact angle of the solid wall with fluids is set to $\theta = 45^\circ$. The wetting boundary condition is prescribed using the geometrical scheme [70,71].

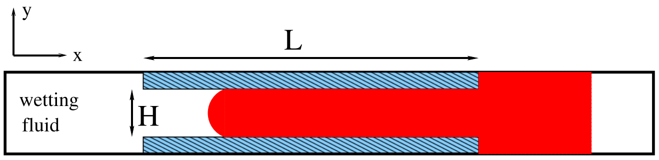

FIG. 14. Schematic of the capillary intrusion test. A wall tube of length $L = 400$ is placed at each side of the lateral edges with a total system length being $2L$ in the x direction. The walls are separated by a distance $H = 20$. Initially, the nonwetting (red) fluid is placed inside the system from $x = 240$ to $x = 750$ while rest of the pore space is filled with the wetting fluid. Periodic boundary conditions are applied everywhere.

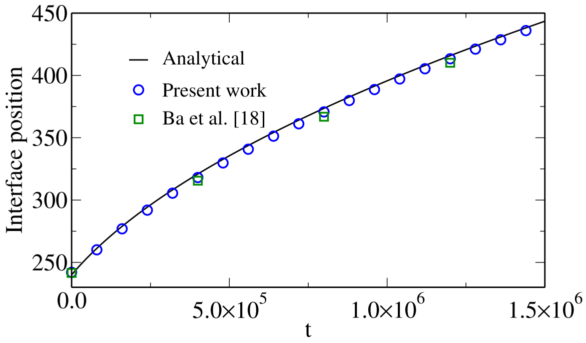

FIG. 15. Position of the interface in the capillary intrusion test with dynamic viscosity ratio of 10 ($\rho_\mathrm{B} = 10$, $\rho_\mathrm{R} = 1$, $\nu_\mathrm{B} = \nu_\mathrm{R} = 0.1$). The interface position found from the reference [18] and present model are in agreement with the analytical prediction.

Given the net surface tension force acting on the blue fluid, it starts to displace the other fluid. Under the assumption that inertial forces are much mess compared to the viscous ones, or Reynolds number is relatively small, the rate of advancement of the fluid interface can be derived as [72,73]

$$V = \frac{\sigma H \cos\theta}{6[\mu_\mathrm{B} x + \mu_\mathrm{R}(L - x)]}, \tag{57}$$

where x is the distance of the fluid-fluid interface measured from the end of solid walls. Equation (57) is derived by a consideration of momentum balance where a Poiseuille type of velocity field distribution is assumed inside the capillary tube [72,73]. The velocity of the interface when it reaches half way in the solid wall ($x = L/2$) is given by $V_m = \frac{1}{6}\frac{\sigma\cos\theta}{\mu_\mathrm{eff}}$ with $\mu_\mathrm{eff} = (\mu_\mathrm{B} + \mu_\mathrm{R})/2$. The corresponding capillary number is then defined as Ca $= \frac{\mu_\mathrm{eff} V_m}{\sigma} = \frac{1}{6}\frac{H\cos\theta}{L} = 5.8 \times 10^{-3}$. First, we choose $\rho_\mathrm{B} = 10$, $\rho_\mathrm{R} = 1$, and $\nu_\mathrm{B} = \nu_\mathrm{R} = 0.1$. The position of the advancing interface as a function of time is shown in Fig. 15. The interface position predicted by Eq. (57) agrees well with the present and the reference model [18]. Note that the analytical solution, Eq. (57) is plotted with the dynamic contact angle $\theta_d = 46.9^\circ$ which is slightly different from the prescribed contact angle $\theta = 45^\circ$.

Next the density ratio is set to $\rho_\mathrm{B}/\rho_\mathrm{R} = 10^3$ and the kinematic viscosity ratio to $\nu_\mathrm{B}/\nu_\mathrm{R} = 0.1$. Figure 16 shows that for the present model still is in agreement with the prediction of

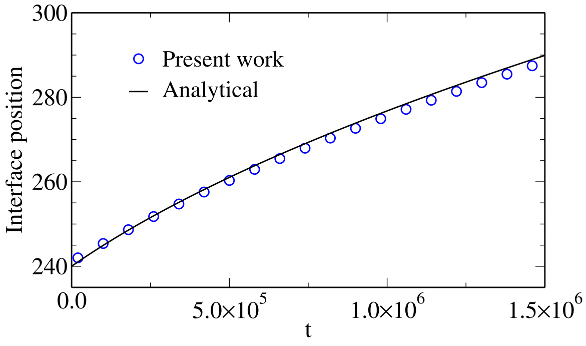

FIG. 16. Position of the interface in the capillary intrusion test for density ratio of 10^3. The simulated interface position is still in good agreement with the analytical prediction.

Eq. (57). At this density ratio, we could not produce stable numerical results from the reference model [18]. The analytical prediction is corrected for the contact dynamic angle of $\theta_d = 47.6^\circ$.

V. DISCUSSION AND CONCLUSIONS

Two-phase flow simulations at high-density and high-viscosity ratios still remain a challenge for the LB models, especially at high Reynolds numbers. To address this issue, we present a model in one class of multicomponent LB simulation, namely the CG or the chromodynamic method.

We adapt a velocity-based equilibrium distribution function for the color-blind fluid populations that was first proposed for the single-phase fluids [36] and later employed for the phase-field LB models [37]. The model of Zu and He [37] uses an explicit fourth-order Cahn-Hilliard scheme to track the interface. Solution of such a scheme using LB equation requires construction and computation of a rather elaborate equilibrium distribution function. Here the interface tracking is taken care by a simple and efficient segregation operator which makes use of post-collision color-blind fluid populations. Existing CG models use ideal gas relation in the bulk-two phase system. To maintain the pressure force balance across a planar fluid-fluid interface, the lattice speed of sound in individual phases must satisfy $\rho_l c_{\mathrm{s,l}}^2 = \rho_h c_{\mathrm{s,h}}^2$ where the subscripts l and h stand for the light and heavy fluids respectively. One of the consequence of this relation is that lattice speed of sound in the heavier fluid $c_{\mathrm{s,h}} = \sqrt{\frac{\rho_l}{\rho_h}} c_{\mathrm{s,l}}$ can get much smaller than $c_{\mathrm{s,l}}$ for high-density ratios. To satisfy the low Mach number assumption $\frac{|\mathbf{u}|}{c_{\mathrm{s,h}}} \ll 1$, the maximum allowed velocity $|\mathbf{u}|$ in the heavier phase is limited by the density ratio. One of the reasons for numerical instability of CG models employing ideal gas relation for the bulk pressure definition is attributed to this effect [41]. Here, the velocity-based formulation of the equilibrium distribution function allows to decouple density and pressure in the bulk phases, thereby removing constraints related to the density ratio.

The CG model has been extensively applied to various steady and unsteady flow situations. Despite its use as a popular tool, a careful analysis of the segregation rule has attracted attention only recently [51,53]. In this work, we further explore the segregation rule for a general case of density contrast while taking into account the nonequilibrium fluid populations. Using a recursive LB equation for the color-blind fluid populations (with the Taylor expansion around the equilibrium fluid populations up to second order in space and time), we discuss the dynamics of the color evolution. Specifically, we show that the color field follows a conservative AC equation with a source term that scales as $\mathcal{O}(\delta t^2 + \mathrm{Ma}^2 \delta t)$. In line with the previous works aimed at analyzing the color dynamics [50,51,53,74], we find that the color indeed satisfies the kinematic condition at the interface within the implicit diffuse interface nature of the model. Further, we show that the present approach allows to tune the numerical mobility of the interface independently of the fluid density ratio. Tunable interface mobility plays an important role in dealing with flow situations with large capillary numbers [51].

The similarity between the interface tracking schemes of the CG and the AC phase-field models is remarkable. Both models neglect the constraint of the thermodynamic consistency and asymptotically solve the fluid dynamical equations in the isothermal regime. The formulaic segregation operator, responsible for the implicit interface tracking in the CG model, was proposed by D'Ortona [10] in 1995. It was built upon the principle that the recoloring should take place only in the interface region and the individual microscopic fluid populations should be redistributed proportionally to the projection of the color gradient on the lattice direction. This principle naturally conserves the local mass and the combined momentum of the fluids. However, the nonconservative AC equation has been used in the study of solidification phenomena for the last five decades [75]. This nonconservative form of the AC equation is derived from the minimization of the free energy functional and includes the contribution of interface curvature to the interface motion. Later, Sun and Beckermann [76] formulated an AC equation where the curvature contribution to the interface motion is negated by the inclusion of a correction term. Finally, Lee and Lin [77] improved upon the work of Sun and Beckermann to propose a locally conservative AC equation. In this context, it is noteworthy that phase-field LB models that prescribe an explicit interface tacking equation have realized the advantage of the locally conservative AC type of equation [33,35] over the more conventional Cahn-Hilliard one [37,48], in terms of the numerical efficiency and low numerical dispersion, only in the last few years.

Given that the intrinsic segregation step remains the same, the present model preserves the usual computational efficiency of the CG models. A known problem that plagues the CG models is high spurious currents in the vicinity of the interface [18,20,61,78]. The velocity-based formulation of the equilibrium distribution considered here results in lower spurious currents than the existing CG models, especially at high-density ratios. The numerical tests show that the model produces accurate results for a wide range of viscosity and density ratios (up to 10^3) at a range of Reynolds numbers (0.01 to 3×10^3), thus expanding the applicability of the CG models.

ACKNOWLEDGMENTS

Support from the Agentur für Arbeit Karlsruhe-Rastatt is gratefully acknowledged. Critical suggestions from Sumesh P. Thampi and Madivala G. Basavaraj are gratefully acknowledged.

APPENDIX: DYNAMICS OF THE COLOR-BLIND FLUID

In this section we show that the equilibrium distribution given by Eq. (4) satisfies the continuity and Navier-Stokes equations. We assume that the time derivative of the force $\mathbf{F}'$, and therefore the microscopic lattice force term F_i are much smaller than the spatial derivatives. Next, we note the following relations, obtained by applying the total differential operator $D_i = \partial_t + \mathbf{c}_i \cdot \nabla$ to Eqs. (4) and (10):

$$\sum_i D_i N_i^{\text{eq}} = \nabla \cdot \mathbf{u}, \tag{A1}$$

$$\sum_i D_i N_i^{\text{eq}} \mathbf{c}_i = \partial_t \mathbf{u} + \nabla \cdot \mathbf{\Pi}^{(0)}, \tag{A2}$$

$$\sum_i D_i^2 N_i^{\text{eq}} = 2\partial_t (\nabla \cdot \mathbf{u}) + \nabla \cdot \nabla \cdot \mathbf{\Pi}^{(0)}, \tag{A3}$$

$$\sum_i D_i^2 N_i^{\text{eq}} \mathbf{c}_i = \partial_t^2 \mathbf{u} + 2\partial_t \nabla \cdot \mathbf{\Pi}^{(0)} + \nabla \cdot \nabla \cdot \mathbf{\Pi}^{(1)}, \tag{A4}$$

$$\sum_i D_i F_i = \nabla \cdot \frac{\mathbf{F}'}{\rho}, \tag{A5}$$

$$\sum_i D_i F_i \mathbf{c}_i = \partial_t \frac{\mathbf{F}'}{\rho}, \tag{A6}$$

where (using Einstein summation convention)

$$\mathbf{\Pi}^{(0)} = \sum_i N_i^{\text{eq}} c_{i\alpha} c_{i\beta} = p\delta_{\alpha\beta} + u_\alpha u_\beta, \tag{A7}$$

$$\mathbf{\Pi}^{(1)} = \sum_i N_i^{\text{eq}} c_{i\alpha} c_{i\beta} c_{i\gamma} \tag{A8}$$

$$= (\delta_{\alpha\beta} u_\gamma + \delta_{\beta\gamma} u_\alpha + \delta_{\gamma\alpha} u_\beta) c_s^2. \tag{A9}$$

To arrive at the continuity equation, we take the zeroth moment of Eq. (37) with respect to the lattice velocities and sum it over all the lattice directions, and use Eqs. (A1), (A3), and (A5), to yield

$$\nabla \cdot \mathbf{u} = \delta t \left(\tau - \tfrac{1}{2}\right)[\nabla \cdot \mathbf{Eu} + \partial_t \nabla \cdot \mathbf{u}], \tag{A10}$$

where

$$\mathbf{Eu} = \partial_t \mathbf{u} + \nabla \cdot \mathbf{\Pi}^{(0)} - \frac{\mathbf{F}'}{\rho}, \tag{A11}$$

represents the Eulerian terms in the Navier-Stokes equations within the correction forces. For further simplification, consideration of the momentum balance is needed. To this end, the first moment of Eq. (37) with respect to the lattice velocities and using Eq. (17) gives

$$\begin{aligned}\mathbf{Eu} = \delta t \left(\tau - \frac{1}{2}\right) \partial_t \mathbf{Eu} + \delta t \left(\tau - \frac{1}{2}\right) \partial_t \nabla \cdot \mathbf{\Pi}^{(0)} \\ + \delta t \nabla \cdot \left(\tau - \frac{1}{2}\right) \nabla \cdot \mathbf{\Pi}^{(1)},\end{aligned} \tag{A12}$$

where we have used Eqs. (A2), (A4), and (A6). Now, using Eqs. (A12) and (A10) in Eq. (A10) yields

$$\nabla \cdot \mathbf{u} = 0 + \mathcal{O}(\delta t^2). \tag{A13}$$

Thus, the color-blind fluid satisfies the incompressibility condition within $\mathcal{O}(\delta t^2)$. For recovering the Navier-Stokes equations we note additional approximations for the incompressible fluids. For incompressible flows, the pressure and velocity fluctuations of the second order in Mach number [58,59], i.e.,

$$\begin{aligned}\partial_t p = \mathcal{O}(\text{Ma}^2), \\ \partial_t \mathbf{uu} = \mathcal{O}(\text{Ma}^2).\end{aligned} \tag{A14}$$

Finally, using Eqs. (A13), (11), and (A14) in Eq. (A12) gives the Navier-Stokes equation

$$\begin{aligned}\rho(\partial_t \mathbf{u} + \nabla \cdot \mathbf{uu}) = -\nabla p_h + \nabla \cdot \mu(\nabla \mathbf{u} + \mathbf{u}\nabla) + \mathbf{F}_s + \mathbf{F}_b \\ + \mathcal{O}(\delta^2 + \text{Ma}^2 \delta t).\end{aligned} \tag{A15}$$

---

[1] J. E. Pilliod and E. G. Puckett, J. Comput. Phys. **199**, 465 (2004).
[2] E. Olsson and G. Kreiss, J. Comput. Phys. **210**, 225 (2005).
[3] X. Shan and H. Chen, Phys. Rev. E **47**, 1815 (1993).
[4] A. K. Gunstensen, D. H. Rothman, S. Zaleski, and G. Zanetti, Phys. Rev. A **43**, 4320 (1991).
[5] M. R. Swift, E. Orlandini, W. R. Osborn, and J. M. Yeomans, Phys. Rev. E **54**, 5041 (1996).
[6] J. Y. Shao, C. Shu, H. B. Huang, and Y. T. Chew, Phys. Rev. E **89**, 033309 (2014).
[7] H. Liang, B. C. Shi, Z. L. Guo, and Z. H. Chai, Phys. Rev. E **89**, 053320 (2014).
[8] D. H. Rothman and J. M. Keller, J. Stat. Phys. **52**, 1119 (1988).
[9] T. Reis and T. N. Phillips, J. Phys. A: Math. Theor. **40**, 4033 (2007).
[10] U. D'Ortona, D. Salin, M. Cieplak, R. B. Rybka, and J. R. Banavar, Phys. Rev. E **51**, 3718 (1995).
[11] M. Latva-Kokko and D. H. Rothman, Phys. Rev. E **71**, 056702 (2005).
[12] A. Montessori, M. Lauricella, M. La Rocca, S. Succi, E. Stolovicki, R. Ziblat, and D. Weitz, Comput. Fluids **167**, 33 (2018).
[13] H. Li, C. Pan, and C. T. Miller, Phys. Rev. E **72**, 026705 (2005).
[14] H. Huang, J.-J. Huang, and X.-Y. Lu, Comput. Fluids **93**, 164 (2014).
[15] D. Grunau, S. Chen, and K. Eggert, Phys. Fluids **5**, 2557 (1993).
[16] G. Rannou, Lattice-Boltzmann method and immiscible two-phase flow, Master's thesis, Georgia Institute of Technology (2008).
[17] H. Huang, J.-J. Huang, X.-Y. Lu, and M. C. Sukop, Int. J. Mod. Phys. C **24**, 1350021 (2013).
[18] Y. Ba, H. Liu, Q. Li, Q. Kang, and J. Sun, Phys. Rev. E **94**, 023310 (2016).
[19] Z. X. Wen, Q. Li, Y. Yu, and K. H. Luo, Phys. Rev. E **100**, 023301 (2019).
[20] S. Leclaire, N. Pellerin, M. Reggio, and J.-Y. Trépanier, Int. J. Multiphase Flow **57**, 159 (2013).
[21] D. J. Holdych, D. Rovas, J. G. Georgiadis, and R. O. Buckius, Int. J. Mod. Phys. C **09**, 1393 (1998).

[22] N. A. C. Sidik and T. Tanahashi, Jurnal Mekanikal **24** (2007).
[23] S. Leclaire, A. Parmigiani, O. Malaspinas, B. Chopard, and J. Latt, Phys. Rev. E **95**, 033306 (2017).
[24] S. Saito, Y. Abe, and K. Koyama, Phys. Rev. E **96**, 013317 (2017).
[25] S. Saito, A. De Rosis, A. Festuccia, A. Kaneko, Y. Abe, and K. Koyama, Phys. Rev. E **98**, 013305 (2018).
[26] S. V. Lishchuk, I. Halliday, and C. M. Care, Phys. Rev. E **77**, 036702 (2008).
[27] Q. Li, K. H. Luo, and X. J. Li, Phys. Rev. E **87**, 053301 (2013).
[28] A. Xu, T. Zhao, L. An, and L. Shi, Int. J. Heat Fluid Flow **56**, 261 (2015).
[29] Q. Li, K. Luo, Q. Kang, Y. He, Q. Chen, and Q. Liu, Prog. Energy Combust. Sci. **52**, 62 (2016).
[30] D. Lycett-Brown and K. H. Luo, Phys. Rev. E **94**, 053313 (2016).
[31] G. Wang, L. Fei, and K. H. Luo, Phys. Rev. Fluids **5**, 083602 (2020).
[32] G. Wang, J. Gao, and K. H. Luo, Phys. Rev. Fluids **5**, 123605 (2020).
[33] A. Fakhari, T. Mitchell, C. Leonardi, and D. Bolster, Phys. Rev. E **96**, 053301 (2017).
[34] H. Wang, X. Yuan, H. Liang, Z. Chai, and B. Shi, Capillarity **2**, 33 (2019).
[35] H. Liang, J. Xu, J. Chen, H. Wang, Z. Chai, and B. Shi, Phys. Rev. E **97**, 033309 (2018).
[36] Z. Guo, B. Shi, and N. Wang, J. Comput. Phys. **165**, 288 (2000).
[37] Y. Q. Zu and S. He, Phys. Rev. E **87**, 043301 (2013).
[38] P. L. Bhatnagar, E. P. Gross, and M. Krook, Phys. Rev. **94**, 511 (1954).
[39] T. Krüger, H. Kusumaatmaja, A. Kuzmin, O. Shardt, G. Silva, and E. M. Viggen, *The Lattice Boltzmann Method* (Springer, Berlin, 2017).
[40] Z. Guo, C. Zheng, and B. Shi, Phys. Rev. E **65**, 046308 (2002).
[41] S. Leclaire, M. Reggio, and J.-Y. Trépanier, Comput. Fluids **48**, 98 (2011).
[42] H. Liu, A. J. Valocchi, and Q. Kang, Phys. Rev. E **85**, 046309 (2012).
[43] D. H. Rothman and S. Zaleski, *Lattice-Gas Cellular Automata: Simple Models of Complex Hydrodynamics* (Cambridge University Press, Cambridge, UK, 2004), Vol. 5.
[44] S. V. Lishchuk, C. M. Care, and I. Halliday, Phys. Rev. E **67**, 036701 (2003).
[45] C. Beckermann, H.-J. Diepers, I. Steinbach, A. Karma, and X. Tong, J. Comput. Phys. **154**, 468 (1999).
[46] I. Steinbach, Modell. Simul. Mater. Sci. Eng. **17**, 073001 (2009).
[47] D. Jacqmin, J. Comput. Phys. **155**, 96 (1999).
[48] H. W. Zheng, C. Shu, and Y. T. Chew, Phys. Rev. E **72**, 056705 (2005).
[49] S. P. Thampi, S. Ansumali, R. Adhikari, and S. Succi, J. Comput. Phys. **234**, 1 (2013).
[50] I. Halliday, A. P. Hollis, and C. M. Care, Phys. Rev. E **76**, 026708 (2007).
[51] A. Subhedar, A. Reiter, M. Selzer, F. Varnik, and B. Nestler, Phys. Rev. E **101**, 013313 (2020).
[52] D. H. Rothman and S. Zaleski, Rev. Mod. Phys. **66**, 1417 (1994).
[53] K. Burgin, J. Spendlove, X. Xu, and I. Halliday, Phys. Rev. E **100**, 043310 (2019).
[54] D. J. Holdych, D. R. Noble, J. G. Georgiadis, and R. O. Buckius, J. Comput. Phys. **193**, 595 (2004).
[55] A. J. Wagner, Phys. Rev. E **74**, 056703 (2006).
[56] D. Lycett-Brown and K. H. Luo, Phys. Rev. E **91**, 023305 (2015).
[57] E. Viggen, The lattice Boltzmann method: Fundamentals and acoustics, Ph.D. thesis, Norwegian University of Science and Technology, Trondheim, Norway (2014).
[58] T. Lee and C.-L. Lin, J. Comput. Phys. **206**, 16 (2005).
[59] A. Majda and J. Srthian, Combust. Sci. Technol. **42**, 185 (1985).
[60] A. C. Monsees, A. Subhedar, B. Busch, B. Nestler, and C. Hilgers, Oil Gas, 28 (2020).
[61] I. Halliday, S. Lishchuk, T. Spencer, K. Burgin, and T. Schenkel, Comput. Phys. Commun. **219**, 286 (2017).
[62] A. J. C. Ladd, J. Fluid Mech. **271**, 285 (1994).
[63] M. Geier, A. Fakhari, and T. Lee, Phys. Rev. E **91**, 063309 (2015).
[64] B. Chopard and M. Droz, *Cellular Automata Modeling of Physical Systems*, Collection Alea-Saclay: Monographs and Texts in Statistical Physics (Cambridge University Press, Cambridge, UK, 1998).
[65] X. He, S. Chen, and R. Zhang, J. Comput. Phys. **152**, 642 (1999).
[66] F. Ren, B. Song, M. C. Sukop, and H. Hu, Phys. Rev. E **94**, 023311 (2016).
[67] S. Leclaire, N. Pellerin, M. Reggio, and J.-Y. Trépanier, Int. J. Numer. Methods Fluids **77**, 732 (2015).
[68] E. Dinesh Kumar, S. A. Sannasiraj, and V. Sundar, Phys. Fluids **31**, 072103 (2019).
[69] S. Chibbaro, Eur. Phys. J. E **27**, 99 (2008).
[70] H. Liu, Y. Ju, N. Wang, G. Xi, and Y. Zhang, Phys. Rev. E **92**, 033306 (2015).
[71] H. Ding and P. D. M. Spelt, Phys. Rev. E **75**, 046708 (2007).
[72] F. Diotallevi, L. Biferale, S. Chibbaro, A. Lamura, G. Pontrelli, M. Sbragaglia, S. Succi, and F. Toschi, Eur. Phys. J.: Spec. Top. **166**, 111 (2009).
[73] C. M. Pooley, H. Kusumaatmaja, and J. M. Yeomans, Eur. Phys. J.: Spec. Top. **171**, 63 (2009).
[74] D. Kehrwald, Numerical analysis of immiscible lattice BGK, Ph.D. thesis, Fraunhofer-Institut für Techno- und Wirtschaftsmathematik, Kaiserslautern, Germany (2002).
[75] W. J. Boettinger, J. A. Warren, C. Beckermann, and A. Karma, Annu. Rev. Mater. Res. **32**, 163 (2002).
[76] Y. Sun and C. Beckermann, J. Comput. Phys. **220**, 626 (2007).
[77] P.-H. Chiu and Y.-T. Lin, J. Comput. Phys. **230**, 185 (2011).
[78] J. Spendlove, X. Xu, O. J. Halliday, T. Schenkel, and I. Halliday, Phys. Rev. E **102**, 013309 (2020).